

# Points2Surf

## Learning Implicit Surfaces from Point Clouds

Anonymous ECCV submission

Paper ID 2941

**Abstract.** A key step in any scanning-based asset creation workflow is to convert unordered point clouds to a surface. Classical methods (e.g., Poisson reconstruction) start to degrade in the presence of noisy and partial scans. Hence, deep learning based methods have recently been proposed to produce complete surfaces, even from partial scans. However, such data-driven methods struggle to generalize to new shapes with large geometric and topological variations. We present POINTS2SURF, a novel *patch-based* learning framework that produces accurate surfaces directly from raw scans without normals. Learning a prior over a combination of detailed local patches and coarse global information improves generalization performance and reconstruction accuracy. Our extensive comparison on both synthetic and real data demonstrates a clear advantage of our method over state-of-the-art alternatives on previously unseen classes (on average, POINTS2SURF brings down reconstruction error by 30% over SPR and by 270%+ over deep learning based SotA methods). Our source code, pre-trained model, and dataset will be made publicly available.

**Keywords:** surface reconstruction, implicit surfaces, point clouds, patch-based, local and global, deep learning, generalization

## 1 Introduction

Converting unstructured point clouds to surfaces is a key step of most scanning-based asset creation workflows, including games and AR/VR applications. While scanning technologies have become more easily accessible (e.g., depth cameras on smart phones, portable scanners), algorithms for producing a surface mesh remain limited. A good surfacing algorithm should be able to handle raw point clouds with noisy and varying sampling density, work with different surface topologies, and generalize across a large range of scanned shapes.

Screened Poisson Reconstruction (SPR) [19] is the most commonly used method to convert an unstructured point cloud, along with its per-point normals, to a surface mesh. While the method is general, in absence of any data-priors, SPR typically produces smooth surfaces, can incorrectly close off holes and tunnels in noisy or non-uniformly sampled scans (see Figure 1), and further degenerates when per-point normal estimates are erroneous.

Hence, several data-driven alternatives [21, 8, 30, 13] have recently been proposed. These methods specialize to particular object categories (e.g., cars, planes,

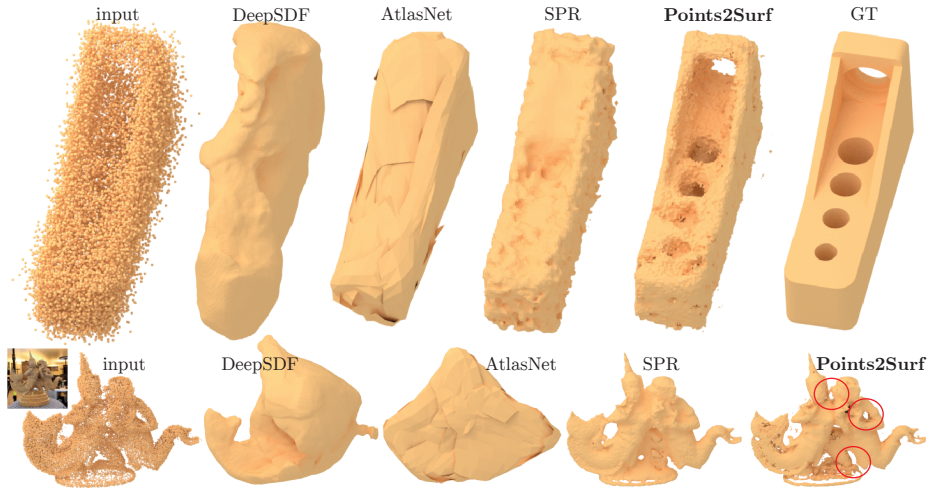


**Fig. 1.** We present POINTS2SURF, a method to reconstruct an accurate implicit surface from a noisy point cloud. Unlike current data-driven surface reconstruction methods like DeepSDF and AtlasNet, it is patch-based, improves detail reconstruction, and unlike Screened Poisson Reconstruction (SPR), a learned prior of low-level patch shapes improves reconstruction accuracy. Note the quality of reconstructions, both geometric and topological, against the original surfaces. The ability of POINTS2SURF to generalize to new shapes makes it the first learning-based approach with significant generalization ability under both geometric and topological variations.

chairs), and typically regress a global latent vector from any input scan. The networks can then decode a final shape (e.g., a collection of primitives [13] or a mesh [30]) from the estimated global latent vector. While such data-specific approaches handle noisy and partial scans, the methods do *not* generalize to new surfaces with varying shape and topology (see Figure 1).

As a solution, we present POINTS2SURF, a method that learns to produce implicit surfaces directly from raw point clouds. During test time, our method can reliably handle raw scans to reproduce fine-scale data features even from noisy and non-uniformly sampled point sets, works for objects with varying topological attributes, and generalizes to new objects (see Figure 1).

Our key insight is to decompose the problem into learning a global and a local function. For the global function, we learn the sign (i.e., inside or outside) of an implicit signed distance function, while, for the local function, we use a patch-based approach to learn absolute distance fields with respect to local point cloud patches. The global task is coarse (i.e., to learn the inside/outside of objects) and hence can be generalized across significant shape variations. The local task exploits the geometric observation that a large variety of shapes can be expressed in terms of a much smaller collection of atomic shape patches [2], which generalizes across arbitrary shapes. We demonstrate that such a factorization leads to a simple, robust, and generalizable approach to learn an implicit signed distance field, from which a final surface is extracted using marching cubes [23].

We test our algorithms on a range of synthetic and real examples, compare on unseen classes against both classical (reduction in reconstruction error by 30% over SPR) and learning based strong baselines (reduction in reconstruction error by 470% over DeepSDF [30] and 270% over AtlasNet [13]), and provide ablations studies. We consistently demonstrate both qualitative and quantitative improvement over all the methods that can be applied directly on raw scans.

## 2 Related Work

Several methods have been proposed to reconstruct surfaces from point clouds. We divide these into methods that aggregate information from a large dataset into a data-driven prior, and methods that do not use a data-driven prior.

*Non-data-driven surface reconstruction.* Berger et al. [4] present an in-depth survey that is focused primarily on non-data-driven methods. Here we focus on approaches that are most relevant to our method.

Scale space meshing [10] applies iterative mean curvature motion to smooth the points for meshing and maps the original points onto it. It is capable of extracting multi-resolution features well. Ohrhallinger et al. propose a combinatorial method [27] which compares favorably with previous methods such as Wrap [11], TightCocone [9] and Shrink [5] especially for sparse sampling and thin structures. However, these methods are not designed to process noisy point clouds.

Another line of work deforms initial meshes [33, 22] or parametric patches [36] to fit a noisy point cloud. These approaches however, cannot change the topology and connectivity of the original meshes or patches, usually resulting in a different connectivity or topology than the ground truth.

The most widely-used approaches to reconstruct surfaces with arbitrary topology from noisy point clouds fit implicit functions to the point cloud and generate a surface as a level set of the function. Early work by Hoppe et al. introduced this approach [16], and since then several methods have focused on different representations of the implicit functions, like Fourier coefficients [17], wavelets [24], radial-basis functions [29] or multi-scale approaches [28, 26]. Alliez et al. [1] use a PCA of 3D Voronoi cells to estimate gradients and fit an implicit function by solving an eigenvalue problem. This approach tends to over-smooth geometric detail. Poisson reconstruction [18, 19] is the current gold standard for non-data-driven surface reconstruction from point clouds. None of the above methods make use of a prior that distills information about typical surface shapes from a large dataset. Hence, while they are very general, they fail to handle partial and/or noisy input. We provide extensive comparisons to Screened Poisson Reconstruction (SPR) [19] in Section 4.

*Data-driven surface reconstruction.* Recently, several methods have been proposed to learn a prior of typical surface shapes from a large dataset. Early work was done by Sauerer et al. [21], where a decision tree is trained to predict the

absolute distance part of an SDF, but ground truth normals are still required to obtain the sign (inside/outside) of the SDF. More recent data-driven methods represent surfaces with a single latent feature vector in a learned feature space. An encoder can be trained to obtain the feature vector from a point cloud. The feature representation acts as a strong prior, since only shapes that are representable in the feature space are reconstructed. Early methods use voxel-based representations of the surfaces, with spatial data-structures like octrees offsetting the cost of a full volumetric grid [34, 35]. Scan2Mesh [8] reconstructs a coarse mesh, including vertices and triangles, from a scan with impressive robustness to missing parts. However, the result is typically very coarse and not watertight or manifold, and does not apply to arbitrary new shapes. AtlasNet [13] uses multiple parametric surfaces as representation that jointly form a surface, achieving impressive accuracy and cross-category generalization. More recently, several approaches learn implicit function representations of surfaces [30, 6, 25]. These methods are trained to learn a functional that maps a latent encoding of a surface to an implicit function that can be used to extract a continuous surface. The implicit representation is more suitable for surfaces with complex topology and tends to produce aesthetically pleasing smooth surfaces.

The single latent feature vector that the methods above use to represent a surface acts as a strong prior, allowing these methods to reconstruct surfaces even in the presence of strong noise or missing parts; but it also limits the generality of these methods. The feature space typically captures only shapes that are similar to the shapes in the training set, and the variety of shapes that can be captured by the feature space is limited by the fixed capacity of the latent feature vector. Instead, we propose to decompose the SDF that is used to reconstruct the surface into a coarse global sign and a detailed local absolute distance. Separate feature vectors are used to represent the global and local parts, allowing us to represent detailed local geometry, without losing coarse global information about the shape.

### 3 Method

Our goal is to reconstruct a watertight surface  $S$  from a 3D point cloud  $P = \{p_1, \dots, p_N\}$  that was sampled from the surface  $S$  through a noisy sampling process, like a 3D scanner. We represent a surface as the zero-set of a signed distance function (SDF)  $f_S$ :

$$S = L_0(f_S) = \{x \in \mathbb{R}^3 \mid f_S(x) = 0\}. \quad (1)$$

Recent work [30, 6, 25] has shown that such an implicit representation of the surface is particularly suitable for neural networks, which can be trained as functionals that take as input a latent representation of the point cloud and output an approximation of the SDF:

$$f_S(x) \approx \tilde{f}_P(x) = s_\theta(x|z), \text{ with } z = e_\phi(P), \quad (2)$$

where  $z$  is a latent description of surface  $S$  that can be encoded from the input point cloud with an encoder  $e$ , and  $s$  is implemented by a neural network that

is conditioned on the latent vector  $z$ . The networks  $s$  and  $e$  are parameterized by  $\theta$  and  $\phi$ , respectively. This representation of the surface is continuous, usually produces watertight meshes, and can naturally encode arbitrary topology. Different from non-data-driven methods like Poisson reconstruction [19], the trained network obtains a strong prior from the dataset it was trained on, that allows robust reconstruction of surfaces even from unreliable input, such as noisy and sparsely sampled point clouds. However, encoding the entire surface with a single latent vector imposes limitations on the accuracy and generality of the reconstruction, due to the limited capacity of the latent representation.

In this work, we factorize the SDF into the absolute distance  $f^d$  and the sign of the distance  $f^s$ , and take a closer look at the information needed to approximate each factor. In order to estimate  $\tilde{f}^d(x)$  of the absolute distance at a query point  $x$ , we only need a *local* neighborhood of the query point in the point cloud  $P$ :

$$\tilde{f}_P^d(x) = s_\theta^d(x|z_x^d), \text{ with } z_x^d = e_\phi^d(\mathbf{p}_x^d), \quad (3)$$

where  $\mathbf{p}_x^d \subset P$  is a local neighborhood of the point cloud centered around  $x$ . Estimating the distance from an encoding of a local neighborhood gives us more accuracy than estimating it from an encoding of the entire shape, since the local encoding  $z_x^d$  can more accurately represent the local neighborhood around  $x$  than the global encoding  $z$ . Note that in a point cloud without noise and sufficiently dense sampling, the single closest point  $p^* \subset P$  to the query  $x$  would be enough to obtain a good approximation of the absolute distance. But since we work with noisy and sparsely sampled point clouds, using a larger local neighborhood increases robustness.

In order to estimate the sign  $\tilde{f}^s(x)$  at the query point  $x$ , we need *global* information about the entire shape, since the interior/exterior of a watertight surface cannot be estimated reliably from a local patch. Instead, we take a global sub-sample of the point cloud  $P$  as input:

$$\tilde{f}_P^s(x) = \text{sgn}(\tilde{g}_P^s(x)) = \text{sgn}(s_\theta^s(x|z_x^s)), \text{ with } z_x^s = e_\psi^s(\mathbf{p}_x^s), \quad (4)$$

where  $\mathbf{p}_x^s \subset P$  is a global subsample of the point cloud,  $\psi$  are the parameters of the encoder, and  $\tilde{g}_P^s(x)$  are logits of the probability that  $x$  has a positive sign. Working with logits avoids discontinuities near the surface, where the sign changes. Since it is more important to have accurate information closer to the query point, we sample  $\mathbf{p}_x^s$  with a density gradient that is highest near the query point and falls off with distance from the query point.

We found that sharing information between the two latent descriptions  $z_x^s$  and  $z_x^d$  benefits both the absolute distance and the sign of the SDF, giving us the formulation we use in Points2Surf:

$$(\tilde{f}_P^d(x), \tilde{g}_P^s(x)) = s_\theta(x|z_x^d, z_x^s), \text{ with } z_x^d = e_\phi^d(\mathbf{p}_x^d) \text{ and } z_x^s = e_\psi^s(\mathbf{p}_x^s). \quad (5)$$

We describe the architecture of our encoders and decoder, the training setup, and our patch sampling strategy in more detail in Section 3.1.

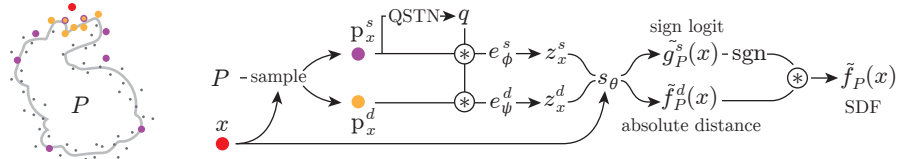


**Fig. 2.** Points2Surf Architecture. Given a query point  $x$  (red) and a point cloud  $P$ , we sample a local patch (yellow) and a coarse global subsample (purple) of the point cloud. These are encoded into two feature vectors that are fed to a decoder, which outputs a logit of the sign probability and the absolute distance of the SDF at the query point  $x$ .

To reconstruct the surface  $S$ , we apply Marching Cubes [23] to a sample grid of the estimated SDF  $\tilde{f}^d(x) * \tilde{f}^s(x)$ . In Section 3.2, we describe a strategy to improve performance by only evaluating a subset of the grid samples.

### 3.1 Architecture and Training

Figure 2 shows an overview of the architecture that implements the encoders and the decoder. Our approach estimates the absolute distance  $\tilde{f}_P^d(x)$  and the sign logits  $\tilde{g}_P^s(x)$  at a query point based on two inputs: the query point  $x$  and the point cloud  $P$ .

*Pointset sampling.* The local patch  $\mathbf{p}_x^d$  and the global sub-sample  $\mathbf{p}_x^s$  are both chosen from the point cloud  $P$  based on the query point  $x$ . The set  $\mathbf{p}_x^d$  is made of the  $n_d$  nearest neighbors of the query point (we choose  $n_d = 300$  but also experiment with other values). Unlike a fixed radius, the nearest neighbors are suitable for query points with arbitrary distance from the point cloud. The global sub-sample  $\mathbf{p}_x^s$  is sampled from  $P$  with a density gradient that decreases with distance from  $x$ :

$$\rho(p_i) = \frac{v(p_i)}{\sum_{p_j \in P} v(p_j)}, \text{ with } v(p_i) = \left[ 1 - 1.5 \frac{\|p_i - x\|_2}{\max_{p_j \in P} \|p_j - x\|_2} \right]_{0.05}^1, \quad (6)$$

where  $\rho$  is the sample probability for a point  $p_i \in P$ ,  $v$  is the gradient that decreases with distance from  $x$ , and the square brackets denote clamping. The minimum value for the clamping ensures that some far points are taken and the sub-sample can represent a closed object. We sample  $n_s$  points from  $P$  according to this probability (we choose  $n_s = 1000$  in our experiments).

*Pointset normalization.* Both  $\mathbf{p}_x^d$  and  $\mathbf{p}_x^s$  are normalized by centering them at the query point  $x$ , and scaling them to unit radius. After running the network, the estimated distance is scaled back to the original size before comparing to the ground truth. Due to the centering, the query point is always at the origin of the normalized coordinate frame and does not need to be passed explicitly to the network. To normalize the orientation of both point subsets, we use a

270 data-driven approach: a Quaternion Spatial Transformer Network (QSTN) [15]  
 271 takes as input the global subset  $\mathbf{p}_x^s$  and estimates a rotation represented as  
 272 quaternion  $q$  that is used to rotate both point subsets. We take the global subset  
 273 as input, since the global information can help the network with finding a more  
 274 consistent rotation. The QSTN is trained end-to-end with the full architecture,  
 275 without direct supervision for the rotation.

276 *Encoder and decoder architecture.* The local encoder  $e_\phi^d$ , and the global encoder  
 277  $e_\psi^s$  are both implemented as PointNets [31], sharing the same architecture, but  
 278 not the parameters. Following the PointNet architecture, a feature representation  
 279 for each point is computed using 5 MLP layers, with a spatial transformer in  
 280 feature space after the third layer. Each layer except the last one uses batch  
 281 normalization and ReLU. The point feature representations are then aggregated  
 282 into point set feature representations  $z_x^d = e_\phi^d(\mathbf{p}_x^d)$  and  $z_x^s = e_\psi^s(\mathbf{p}_x^s)$  using a  
 283 channel-wise maximum. The decoder  $s_\theta$  is implemented as 4-layer MLP that  
 284 takes as input the concatenated feature vectors  $z_x^d$  and  $z_x^s$  and outputs both the  
 285 absolute distance  $\tilde{f}^d(x)$  and sign logits  $\tilde{g}^s(x)$ .

286 *Losses and training.* We train our networks end-to-end to regress the absolute  
 287 distance of the query point  $x$  from the watertight ground truth surface  $S$  and  
 288 classify the sign as positive (outside  $S$ ) or negative (inside  $S$ ). We assume that  
 289 ground truth surfaces are available during training for supervision. We use an  $L_2$   
 290 regression for the absolute distance:

$$\mathcal{L}^d(x, P, S) = \|\tilde{f}_P^d(x) - d(x, S)\|_2, \quad (7)$$

291 where  $d(x, S)$  is the distance of  $x$  to the ground truth surface  $S$ . For the sign  
 292 classification, we use the binary cross entropy  $H$  as loss:

$$\mathcal{L}^s(x, P, S) = H\left(\sigma(\tilde{g}_P^s(x)), [f_S(x) > 0]\right), \quad (8)$$

300 where  $\sigma$  is the logistic function to convert the sign logits to probabilities, and  
 301  $[f_S(x) > 0]$  is 1 if  $x$  is outside the surface  $S$  and 0 otherwise. In our optimization,  
 302 we minimize these two losses for all shapes and query points in the training set:  
 303

$$\sum_{(P, S) \in \mathcal{S}} \sum_{x \in \mathcal{X}_S} \mathcal{L}^d(x, P, S) + \mathcal{L}^s(x, P, S), \quad (9)$$

304 where  $\mathcal{S}$  is the set of surfaces  $S$  and corresponding point clouds  $P$  in the training  
 305 set and  $\mathcal{X}_S$  the set of query points for shape  $S$ . More information about the  
 306 training set we use in our experiments is given in Section 4.

### 311 3.2 Surface Reconstruction

312 At inference time, we want to reconstruct a surface  $\tilde{S}$  from an estimated SDF  
 313  $\tilde{f}(x) = \tilde{f}^d(x)*\tilde{f}^s(x)$ . A straight-forward approach is to apply Marching Cubes [23]

315 to a volumetric grid of SDF samples. Obtaining a high-resolution result, however,  
 316 would require evaluating a prohibitive number of samples for each shape. We  
 317 observe that in order to reconstruct a surface, a Truncated Signed Distance Field  
 318 (TSDF) is sufficient, where the SDF is truncated to the interval  $[-\epsilon, \epsilon]$  (we set  $\epsilon$  to  
 319 three times the grid spacing in all our experiments). We only need to evaluate the  
 320 SDF for samples that are inside this interval, while samples outside the interval  
 321 merely need the correct sign. We leave samples with a distance larger than  $\epsilon$   
 322 to the nearest point in  $P$  blank, and in a second step, we propagate the signed  
 323 distance values from non-blank to blank samples, to obtain the correct sign in  
 324 the truncated regions of the TSDF. We iteratively apply a box filter of size  $3^3$  at  
 325 the blank samples until convergence. In each step, we update initially unknown  
 326 samples only if the filter response is greater than a user-defined confidence  
 327 threshold (we use 13 in our experiments). After each step, the samples are set to  
 328 -1 if the filter response was negative or to +1 for a positive response.

## 330 4 Results

331 We evaluate our method by comparing to SPR as the gold standard for non-  
 332 data-driven surface reconstruction and to two state-of-the-art data-driven surface  
 333 reconstruction methods. We provide both qualitative and quantitative com-  
 334 parisons on several datasets in Section 4.2, and perform an ablation study in  
 335 Section 4.3.

### 338 4.1 Datasets

340 We train and evaluate on the ABC dataset [20] which contains a large number  
 341 and variety of high-quality CAD meshes. We pick 4950 clean watertight meshes  
 342 for training and 100 meshes for the validation and test sets. Note that since we  
 343 operate on local patches, each mesh in the datasets produces a large number of  
 344 diverse training samples. Operating on local patches also allows us to generalize  
 345 to other types of shapes which we demonstrate on two additional datasets that  
 346 we use for testing only: a dataset of 22 diverse meshes which are well-known  
 347 in geometry processing, such as the Utah teapot, the Stanford Bunny and the  
 348 Armadillo, which we call the FAMOUS dataset, and 3 REAL scans of complex  
 349 objects used in several denoising papers [37, 32]. Examples from each dataset  
 350 are shown in Figure 3. The ABC dataset contains predominantly CAD models  
 351 of mechanical parts, while the FAMOUS dataset contains more organic shapes,  
 352 such as characters and animals. Since we train on the ABC dataset, the FAMOUS  
 353 dataset serves to test the generalizability of our method versus baselines.

354  
 355 *Pointcloud sampling.* As a pre-processing step, we center all meshes at the origin  
 356 and scale them uniformly to fit within the unit cube. To obtain point clouds  
 357  $P$  from the meshes  $S$  in the ABC and FAMOUS datasets, we simulate scanning  
 358 them with a time-of-flight sensor from random viewpoints using BlenSor [14].  
 359 BlenSor realistically simulates various types of scanner noise and artifacts such as



**Fig. 3.** Dataset examples. Examples of the ABC dataset and its three point cloud variants are shown on the left, examples of the famous dataset and its five point cloud variants on the right.

backfolding, ray reflections, and per-ray noise. We scan each mesh in the FAMOUS dataset with 10 scans, and each mesh in the ABC dataset with a random number of scans, between 5 and 30. For each scan, we place the scanner at a random location on a sphere centered at the origin, with the radius chosen randomly in  $U[3L, 5L]$ , where  $L$  is the largest side of the mesh bounding box. The scanner is oriented to point at a location with small random offset from the origin, between  $U[-0.1L, 0.1L]$  along each axis, and rotated randomly around the view direction. Each scan has a resolution of  $176 \times 144$ , resulting in roughly 25k points, minus some points missing due to simulated scanning artifacts. The point clouds of multiple scans of a mesh are merged to obtain the final point cloud.

*Dataset variants.* We create multiple different versions of both the ABC and FAMOUS datasets, with different amounts of per-ray noise. Per-ray noise simulates inaccuracies in the depth measurements as Gaussian noise added to the depth values. For the ABC dataset, we create a noise-free version of the point clouds (called ABC *no-noise*), a version with variable amounts of noise where the standard deviation is randomly chosen in  $U[0, 0.05L]$  (ABC *var-noise*), and a version with a constant noise strength of  $0.05L$  (ABC *max-noise*). For the FAMOUS dataset, we create a version without noise (FAMOUS *no-noise*), a version with a medium noise strength  $0.01L$  (FAMOUS *med-noise*), and a version with maximum amount of noise  $0.05L$  (FAMOUS *max-noise*). Additionally we create sparser and denser point clouds by varying the number of scans: a variant with 5 scans instead of 10 (FAMOUS *sparse*), and a version with 30 scans (FAMOUS *dense*), both with a medium noise strength of  $0.01L$ . The training set uses the ABC *var-noise* version, all other variants are used for evaluation only.

*Query points.* The training set also contains a set  $\mathcal{X}_S$  of query points for each (point cloud, mesh) pair  $(P, S) \in \mathcal{S}$ . Query points closer to the surface are more important for the surface reconstruction and more difficult to estimate. Hence, we randomly sample a set of 1000 points on the surface and offset them in the normal direction by a uniform random amount in  $U[-0.02L, 0.02L]$ . An additional 1000 query points are sampled randomly in the unit cube that contains the surface, for a total of 2000 query points per mesh. During training, we randomly sample a subset of 1000 query points per mesh in each epoch.

**Table 1.** Comparison of reconstruction errors. We show the Chamfer distance between reconstructed and ground truth surfaces averaged over all shapes in a dataset. Both the absolute value of the error multiplied by 100 (abs.), and the error relative to Point2Surf (rel.) are shown to facilitate the comparison. Our method consistently performs better than the baselines, due to its strong and generalizable prior.

	DeepSDF	AtlasNet	SPR	POINTS2SURF		
	abs.	rel.	abs.	rel.	abs.	rel.
ABC no-noise	8.41	4.68	4.69	2.61	2.49	1.39
ABC var-noise	12.51	5.86	4.04	1.89	3.29	1.54
ABC max-noise	11.34	4.11	4.47	1.62	3.89	1.41
FAMOUS no-noise	10.08	7.14	4.69	3.33	1.67	1.18
FAMOUS med-noise	9.89	6.57	4.54	3.01	1.80	1.20
FAMOUS max-noise	13.17	5.23	4.14	1.64	3.41	1.35
FAMOUS sparse	10.41	5.41	4.91	2.55	2.17	1.12
FAMOUS dense	9.49	7.15	4.35	3.28	1.60	1.21
<b>average</b>	<b>10.66</b>	<b>5.77</b>	<b>4.48</b>	<b>2.49</b>	<b>2.54</b>	<b>1.30</b>
					<b>1.92</b>	<b>1.00</b>

## 4.2 Comparison to Baselines

We compare our method, both qualitatively and quantitatively, to recent data-driven surface reconstruction methods, AtlasNet [13] and DeepSDF [30], and to SPR [19], which is still the gold standard in non-data-driven surface reconstruction from point clouds. Both AtlasNet and DeepSDF represent a full surface as a single latent vector that is decoded into either a set of parametric surface patches in AtlasNet, or an SDF in DeepSDF. In contrast, SPR solves for an SDF that has a given sparse set of point normals as gradients, and takes on values of 0 at the point locations. We use the default values given by the authors for all baselines and re-train the two data-driven methods on our training set. We provide SPR with point normals as input, which we estimate from the input point cloud using the recent data-driven patch-based method PCPNet [15]. DeepSDF additionally requires an estimate of the SDF’s sign at random samples in the bounding box of a surface. We use the ground truth signed distance for DeepSDF, giving us an upper bound on the reconstruction.

*Error metric.* To measure the reconstruction error of each method, we sample both the reconstructed surface and the ground truth surface with 10k points and compute the Chamfer distance [3, 12] between the two point sets:

$$d_{\text{ch}}(A, B) := \frac{1}{|A|} \sum_{p_i \in A} \min_{p_j \in B} \|p_i - p_j\|_2^2 + \frac{1}{|B|} \sum_{p_j \in B} \min_{p_i \in A} \|p_j - p_i\|_2^2, \quad (10)$$

where  $A$  and  $B$  are point sets sampled on the two surfaces. The Chamfer distance penalizes both false negatives (missing parts) and false positives (excess parts).

*Quantitative and qualitative comparison.* A quantitative comparison of the reconstruction quality is shown in Table 1, and Figure 4 compares a few reconstructions

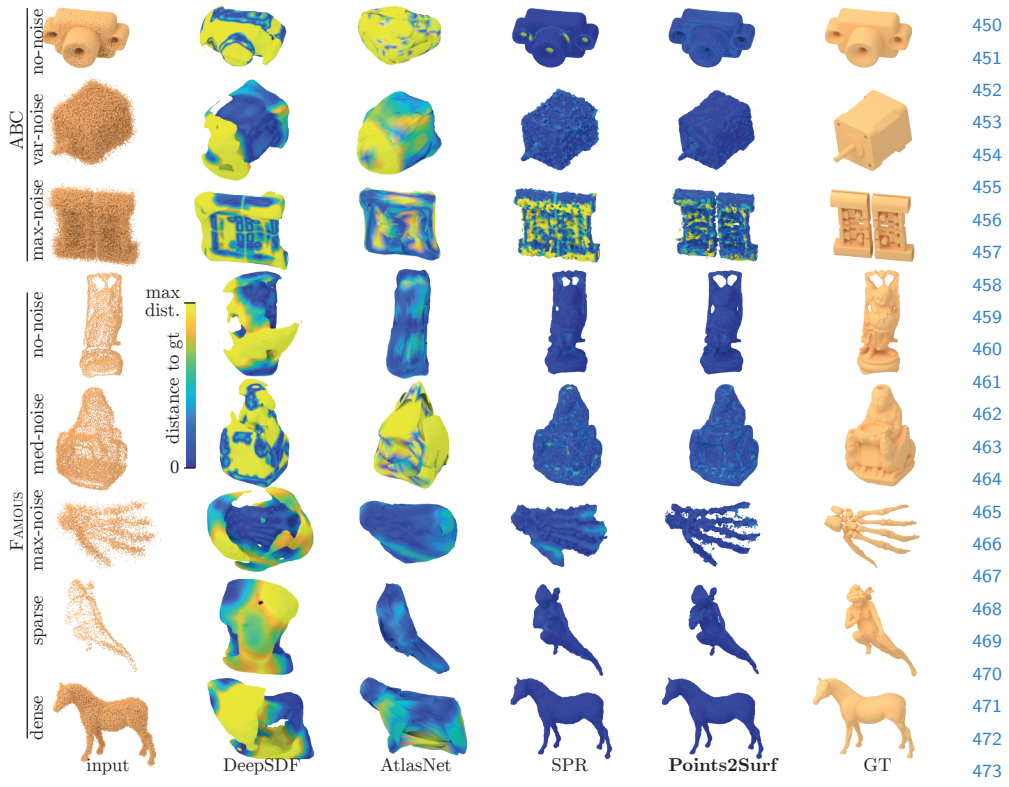


**Fig. 4.** Qualitative comparison of surface reconstructions. We evaluate one example from each dataset variant with each method. Colors show the distance of the reconstructed surface to the ground truth surface.

qualitatively. All methods were trained on the training set of the ABC *var-noise* dataset, which contains CAD models, predominantly of mechanical parts, while the more organic shapes in the FAMOUS dataset test how well each method can generalize to novel types of shapes.

Since neither of the datasets has categories with a high geometric consistency among the shapes, like cars or airplanes, DeepSDF and AtlasNet struggle to accurately encode detailed surfaces in their latent representation and show a significantly higher reconstruction error than SPR or POINTS2SURF. This is also clearly visible in Figure 4, where the surfaces reconstructed by DeepSDF and AtlasNet appear over-smoothed and inaccurate.

In SPR, the full shape space does not need to be encoded into a prior with limited capacity, resulting in a better accuracy. But this lack of a strong prior also prevents SPR from robustly reconstructing typical surface features, such as holes or planar patches (see Figures 1 and 4).

POINTS2SURF learns a prior of local surface detail, instead of a prior for global surface shapes. This local prior helps recover surface detail like holes and

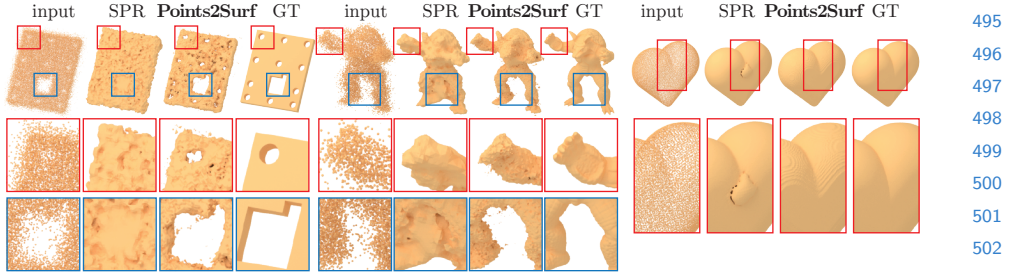


**Fig. 5.** Comparison of reconstruction details. Our learned prior is improves the reconstruction robustness for geometric detail compared to SPR.

planar patches more robustly, improving our accuracy over SPR. Since there is less variety and more consistency in local surface detail compared to global surface shapes. Also, as inaccuracies of local detail result in smaller errors, our method generalizes better and achieves a significantly higher accuracy than the data-driven methods that use a prior over the global surface shape.

*Generalization.* A comparison of our generalization performance against AtlasNet and DeepSDF shows an advantage for our method. In Table 1, we can see that the error for DeepSDF and AtlasNet increases more when going from the ABC dataset to the FAMOUS dataset than the error for our method (DeepSDF and AtlasNet tend to have larger values for the FAMOUS dataset than for the ABC dataset in the relative error columns). This suggests that our method generalizes better from the CAD models in the ABC dataset set to the more organic shapes in the FAMOUS dataset than these two other data-driven methods.

*Topological Quality.* Examples of geometric detail that benefits from our prior are shown in Figure 5. In each example, we compare our POINTS2SURF to SPR, which does not use a learned prior. In the first example on the left, we can see that small features such as holes can be recovered from a very weak geometric signal in a noisy point cloud. Concavities, such as the space between the legs of the Armadillo model, and fine shape details like the Armadillo’s hand are also recovered more accurately in the presence of strong noise. In the heart example on the right, the concavity makes it hard to estimate the correct sign (inside versus outside) based on only a small local neighborhood, leading to erroneous directions for normal estimates leading to an artifact for SPR. In contrast, the global information we use in our patches helps us estimate the correct sign, even if the local neighborhood is misleading.

*Effect of Noise.* Examples of reconstructions from point clouds with increasing amounts of noise are shown in Figure 6. We show both POINTS2SURF and other reconstructions. Our learned prior for local patches and our coarse global surface information makes it easier to find small holes and large concavities. In the medium noise setting, we can recover both the small holes and the large concavity

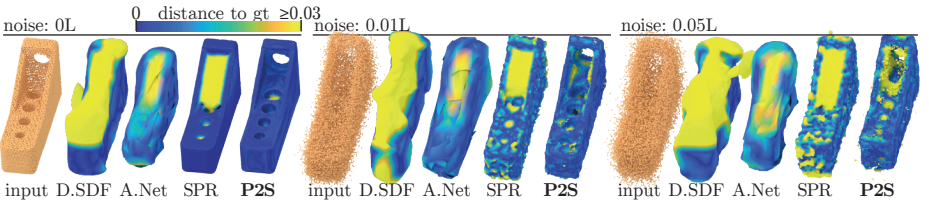


**Fig. 6.** Effect of noise on our reconstruction. DeepSDF (D.SDF), AtlasNet (A.Net), SPR and Point2Surf (P2S) are applied to increasingly noisy point clouds. Our patch-based data-driven approach is more accurate than DeepSDF and AtlasNet, and can more robustly recover small holes and concavities than SPR.

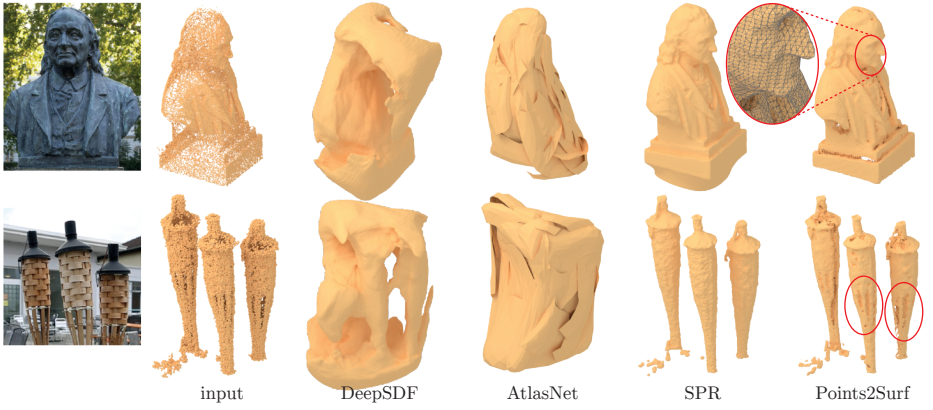


**Fig. 7.** Reconstruction of real-world point clouds. Snapshots of the real-world objects are shown on the left. DeepSDF and AtlasNet do not generalize well, resulting in inaccurate reconstructions, while the smoothness prior of SPR results in loss of detail near concavities and holes. Our data-driven local prior preserves these details more faithfully.

of the surface. In the maximum noise setting, it is very difficult to detect the small holes, but we can still recover the concavity.

*Real-world data.* We reconstruct two point clouds from three multi-view point clouds. The results are shown in Figures 1 and 7. The point clouds in Figure 1 bottom and Figure 7 bottom both originate from a multi-view dataset [37] and were obtained with a plane-sweep algorithm [7] from multiple photographs of an object. We additionally remove outliers using the recent PointCleanNet [32]. Figure 7 top was obtained by the authors through an SfM approach. We compare our results to DeepSDF, AtlasNet and SPR. DeepSDF and AtlasNet do not generalize well to previously unseen shape categories. SPR performs significantly better, its smoothness prior tends to over-smooth shapes and close holes, loosing geometric detail. Points2Surf better preserves holes and details, at the cost of a slight increase in topological noise. Our technique also generalizes to unseen point-cloud acquisition methods.

**Table 2.** Ablation Study. We compare POINTS2SURF to using a fixed radius of small, medium and large size for the local patch instead of the  $k$  nearest neighbors ( $r_{\text{small}}$ ,  $r_{\text{med}}$  and  $r_{\text{large}}$ ); to using a smaller and larger number of nearest neighbors ( $k_{\text{small}}$  and  $k_{\text{large}}$ ); and to using a shared encoder for the local patch  $\mathbf{p}_x^d$  and the global sub-sample  $\mathbf{p}_x^s$  ( $e_{\text{shared}}$ ). We show the Chamfer distance relative to POINTS2SURF. Our design choices perform better than any of these variants on the ABC and FAMOUS datasets.

		$r_{\text{small}}$	$r_{\text{med}}$	$r_{\text{large}}$	$k_{\text{small}}$	$k_{\text{large}}$	$e_{\text{shared}}$	POINTS2SURF
ABC var-noise		1.12	1.07	1.05	1.08	1.87	1.02	<b>1.00</b>
FAMOUS no-noise		1.09	1.08	1.17	1.05	8.10	1.06	<b>1.00</b>
FAMOUS med-noise		1.06	1.05	1.10	1.04	7.89	1.05	<b>1.00</b>
FAMOUS max-noise		1.07	1.19	1.13	1.09	1.79	1.01	<b>1.00</b>
	average	1.08	1.11	1.11	1.07	4.14	1.03	<b>1.00</b>

### 4.3 Ablation Study

We evaluate several design choices we made in our approach using an ablation study, as shown in Table 2. We evaluate the number of nearest neighbors  $k = 300$  we use for the local patch by decreasing and increasing  $k$  by a factor of 4, effectively halving and doubling the size of the local patch. A large  $k$  performs significantly worse because we may lose local detail with a larger patch size, while a small  $k$  still works reasonably well, but gives lower performance especially on large noise settings (FAMOUS max-noise). We also compare POINTS2SURF to using a fixed radius for the local patch, with three different sizes (0.05L, 0.1L and 0.2L). A fixed patch size is less suitable than nearest neighbors when computing the distance at query points that are far away from the surface, giving a lower performance than the standard nearest neighbor setting. Finally, we compare our method to using a single shared encoder for both the global sub-sample  $\mathbf{p}_x^s$  and the local patch  $\mathbf{p}_x^d$ , by concatenating the two before encoding them with a single encoder. The performance of this variant is still competitive, but shows that using two separate encoders increases performance.

## 5 Conclusion

We have presented POINTS2SURF as a method for surface reconstruction from raw point clouds. Our method reliably captures both geometric and topological details, and generalizes to unseen shapes more robustly than current methods.

Although the inferred SDFs are accurate far from the surface, they are noisy near the 0-set, resulting in bumpy surfaces when processing raw point clouds. One interesting next step would be to combine coarse reconstructions with local surface priors to add fine scale details. We believe such an iterative and multiscale approach would further improve the quality of POINTS2SURF, especially by reducing the imperfections in fine-scale details. Finally, where we used Marching Cubes to extract the surface from the inferred SDF, it would be interesting to develop a differentiable version of Marching Cubes, and then jointly train SDF estimation and surface extraction.

## 630 References

- 631 1. Alliez, P., Cohen-Steiner, D., Tong, Y., Desbrun, M.: Voronoi-based variational  
632 reconstruction of unoriented point sets. In: Symposium on Geometry processing.  
633 vol. 7, pp. 39–48 (2007)
- 634 2. Badki, A., Gallo, O., Kautz, J., Sen, P.: Meshlet priors for 3d mesh reconstruction.  
635 ArXiv (2020)
- 636 3. Barrow, H.G., Tenenbaum, J.M., Bolles, R.C., Wolf, H.C.: Parametric correspon-  
637 dence and chamfer matching: Two new techniques for image matching. In: Proceed-  
638 ings of the 5th International Joint Conference on Artificial Intelligence - Volume  
639 2. pp. 659–663. IJCAI’77, Morgan Kaufmann Publishers Inc., San Francisco, CA,  
640 USA (1977), <http://dl.acm.org/citation.cfm?id=1622943.1622971>
- 641 4. Berger, M., Tagliasacchi, A., Seversky, L.M., Alliez, P., Guennebaud, G., Levine,  
642 J.A., Sharf, A., Silva, C.T.: A survey of surface reconstruction from point clouds.  
643 In: Computer Graphics Forum. vol. 36, pp. 301–329. Wiley Online Library (2017)
- 644 5. Chaine, R.: A geometric convection approach of 3-d reconstruction. In: Proceedings  
645 of the 2003 Eurographics/ACM SIGGRAPH symposium on Geometry processing.  
646 pp. 218–229. Eurographics Association (2003)
- 647 6. Chen, Z., Zhang, H.: Learning implicit fields for generative shape modeling. In:  
648 Proc. of CVPR (2019)
- 649 7. Collins, R.T.: A space-sweep approach to true multi-image matching. In: Proceeding  
650 s of the IEEE Computer Society Conference on Computer Vision and Pattern  
651 Recognition. pp. 358–363. IEEE (1996)
- 652 8. Dai, A., Nießner, M.: Scan2mesh: From unstructured range scans to 3d meshes. In:  
653 Proc. Computer Vision and Pattern Recognition (CVPR), IEEE (2019)
- 654 9. Dey, T.K., Goswami, S.: Tight cocone: a water-tight surface reconstructor. In:  
655 Proceedings of the eighth ACM symposium on Solid modeling and applications. pp.  
656 127–134. ACM (2003)
- 657 10. Digne, J., Morel, J.M., Souzani, C.M., Lartigue, C.: Scale space meshing of raw data  
658 point sets. In: Computer Graphics Forum. vol. 30, pp. 1630–1642. Wiley Online  
659 Library (2011)
- 660 11. Edelsbrunner, H.: Surface reconstruction by wrapping finite sets in space. In:  
661 Discrete and computational geometry, pp. 379–404. Springer (2003)
- 662 12. Fan, H., Su, H., Guibas, L.J.: A point set generation network for 3d object recon-  
663 struction from a single image. In: Proceedings of the IEEE conference on computer  
664 vision and pattern recognition. pp. 605–613 (2017)
- 665 13. Groueix, T., Fisher, M., Kim, V.G., Russell, B., Aubry, M.: AtlasNet: A Papier-  
666 Mâché Approach to Learning 3D Surface Generation. In: Proceedings IEEE Conf.  
667 on Computer Vision and Pattern Recognition (CVPR) (2018)
- 668 14. Gschwandtner, M., Kwitt, R., Uhl, A., Pree, W.: Blensor: Blender sensor simulation  
669 toolbox. In: International Symposium on Visual Computing. pp. 199–208. Springer  
670 (2011)
- 671 15. Guerrero, P., Kleiman, Y., Ovsjanikov, M., Mitra, N.J.: PCPNet: Learning local  
672 shape properties from raw point clouds. Computer Graphics Forum **37**(2), 75–85  
673 (2018). <https://doi.org/10.1111/cgf.13343>
- 674 16. Hoppe, H., DeRose, T., Duchamp, T., McDonald, J., Stuetzle, W.: Surface recon-  
675 struction from unorganized points, vol. 26. ACM (1992)
- 676 17. Kazhdan, M.: Reconstruction of solid models from oriented point sets. In: Pro-  
677 ceedings of the third Eurographics symposium on Geometry processing. p. 73.  
678 Eurographics Association (2005)

- 675 18. Kazhdan, M., Bolitho, M., Hoppe, H.: Poisson surface reconstruction. In: Proc. of  
676 the Eurographics symposium on Geometry processing (2006) 675  
677 19. Kazhdan, M., Hoppe, H.: Screened poisson surface reconstruction. ACM Transac-  
678 tions on Graphics (ToG) **32**(3), 29 (2013) 677  
679 20. Koch, S., Matveev, A., Jiang, Z., Williams, F., Artemov, A., Burnaev, E., Alexa, M.,  
680 Zorin, D., Panozzo, D.: Abc: A big cad model dataset for geometric deep learning.  
681 In: The IEEE Conference on Computer Vision and Pattern Recognition (CVPR)  
682 (June 2019) 681  
683 21. Ladicky, L., Saurer, O., Jeong, S., Maninchedda, F., Pollefeys, M.: From point clouds  
684 to mesh using regression. In: Proceedings of the IEEE International Conference on  
685 Computer Vision. pp. 3893–3902 (2017) 682  
686 22. Li, G., Liu, L., Zheng, H., Mitra, N.J.: Analysis, reconstruction and  
687 manipulation using arterial snakes. In: ACM SIGGRAPH Asia 2010  
688 Papers. SIGGRAPH ASIA ’10, Association for Computing Machinery,  
689 New York, NY, USA (2010). <https://doi.org/10.1145/1866158.1866178>,  
690 <https://doi.org/10.1145/1866158.1866178> 683  
691 23. Lorensen, W.E., Cline, H.E.: Marching cubes: A high resolution 3d surface  
692 construction algorithm. In: ACM siggraph computer graphics. vol. 21, pp. 163–169.  
693 ACM (1987) 684  
694 24. Manson, J., Petrova, G., Schaefer, S.: Streaming surface reconstruction using  
695 wavelets. In: Computer Graphics Forum. vol. 27, pp. 1411–1420. Wiley Online  
696 Library (2008) 692  
697 25. Mescheder, L., Oechsle, M., Niemeyer, M., Nowozin, S., Geiger, A.: Occupancy  
698 networks: Learning 3d reconstruction in function space. In: Proc. of CVPR (2019) 693  
699 26. Nagai, Y., Ohtake, Y., Suzuki, H.: Smoothing of partition of unity implicit surfaces  
700 for noise robust surface reconstruction. In: Computer Graphics Forum. vol. 28, pp.  
701 1339–1348. Wiley Online Library (2009) 694  
702 27. Ohrhallinger, S., Mudur, S., Wimmer, M.: Minimizing edge length to connect  
703 sparsely sampled unstructured point sets. Computers & Graphics **37**(6), 645–658  
704 (2013) 695  
705 28. Ohtake, Y., Belyaev, A., Seidel, H.P.: A multi-scale approach to 3d scattered data  
706 interpolation with compactly supported basis functions. In: 2003 Shape Modeling  
707 International. pp. 153–161. IEEE (2003) 696  
708 29. Ohtake, Y., Belyaev, A., Seidel, H.P.: 3d scattered data interpolation and approxi-  
709 mation with multilevel compactly supported rbfs. Graphical Models **67**(3), 150–165  
710 (2005) 697  
711 30. Park, J.J., Florence, P., Straub, J., Newcombe, R., Lovegrove, S.: Deepsdf: Learn-  
712 ing continuous signed distance functions for shape representation. arXiv preprint  
713 arXiv:1901.05103 (2019) 698  
714 31. Qi, C.R., Su, H., Mo, K., Guibas, L.J.: Pointnet: Deep learning on point sets for 3d  
715 classification and segmentation. arXiv preprint arXiv:1612.00593 (2016) 709  
716 32. Rakotosaona, M.J., La Barbera, V., Guerrero, P., Mitra, N.J., Ovsjanikov, M.:  
717 Pointcleanet: Learning to denoise and remove outliers from dense point clouds.  
718 Computer Graphics Forum (2019) 713  
719 33. Sharf, A., Lewiner, T., Shamir, A., Kobbett, L., Cohen-Or, D.: Competing fronts  
720 for coarse-to-fine surface reconstruction. In: Computer Graphics Forum. vol. 25,  
721 pp. 389–398. Wiley Online Library (2006) 715  
722 34. Tatarchenko, M., Dosovitskiy, A., Brox, T.: Octree generating networks: Efficient  
723 convolutional architectures for high-resolution 3d outputs. In: Proceedings of the  
724 IEEE International Conference on Computer Vision. pp. 2088–2096 (2017) 716

- 720 35. Wang, P.S., Sun, C.Y., Liu, Y., Tong, X.: Adaptive o-cnn: A patch-based deep  
721 representation of 3d shapes. ACM Transactions on Graphics (TOG) **37**(6), 1–11  
722 (2018)
- 723 36. Williams, F., Schneider, T., Silva, C.T., Zorin, D., Bruna, J., Panizzo, D.: Deep  
724 geometric prior for surface reconstruction. In: Proceedings of the IEEE Conference  
725 on Computer Vision and Pattern Recognition. pp. 10130–10139 (2019)
- 726 37. Wolff, K., Kim, C., Zimmer, H., Schroers, C., Botsch, M., Sorkine-Hornung, O.,  
727 Sorkine-Hornung, A.: Point cloud noise and outlier removal for image-based 3d  
728 reconstruction. In: 2016 Fourth International Conference on 3D Vision (3DV). pp.  
729 118–127 (Oct 2016). <https://doi.org/10.1109/3DV.2016.20>
- 730
- 731
- 732
- 733
- 734
- 735
- 736
- 737
- 738
- 739
- 740
- 741
- 742
- 743
- 744
- 745
- 746
- 747
- 748
- 749
- 750
- 751
- 752
- 753
- 754
- 755
- 756
- 757
- 758
- 759
- 760
- 761
- 762
- 763
- 764